Journal of Geophysical Research: Oceans

RESEARCH ARTICLE
10.1029/2017JC013320

The Interannual Variability of Sea Surface Temperature in the Red Sea From 35 Years of Satellite and In Situ Observations

Kristopher B. Karnauskas[1,2] and **Burton H. Jones**[3]

[1]Cooperative Institute for Research in Environmental Sciences, University of Colorado Boulder, Boulder, CO, USA, [2]Department of Atmospheric and Oceanic Sciences, University of Colorado Boulder, Boulder, CO, USA, [3]Red Sea Research Center, King Abdullah University of Science and Technology, Thuwal, Kingdom of Saudi Arabia

Key Points:
- The interannual variability of sea surface temperature in the Red Sea is analyzed from 1982 to 2016 using a 28 km satellite/in situ product
- Variability is greatest in the northern Red Sea in wintertime; objective analysis reveals a whole-sea mode and a meridional gradient mode
- Surface heat exchange is a dominant mechanism in both modes; El Niño (North Atlantic Oscillation) impacts the southern (northern) Red Sea

Correspondence to:
K. B. Karnauskas,
kristopher.karnauskas@colorado.edu

Citation:
Karnauskas, K. B., & Jones, B. H. (2018). The interannual variability of sea surface temperature in the Red Sea from 35 years of satellite and in situ observations. *Journal of Geophysical Research: Oceans*, *123*, 5824–5841. https://doi.org/10.1029/2017JC013320

Received 30 JUL 2017
Accepted 16 MAY 2018
Accepted article online 26 MAY 2018
Published online 21 AUG 2018

Abstract Falling between the dynamics of the seasonal cycle and expressions of longer-term trends, the interannual variability of sea surface temperature (SST) in the Red Sea has not received enough attention. With multiple decades of satellite SST observations with spatial resolution capable of resolving patterns of variability within the Red Sea, the time has come for a description and diagnosis of the observed interannual variability of SST in this important semienclosed sea. While interannual variability of SST occurs throughout the Red Sea in both summer and winter, the greatest variability is found in the northern Red Sea during winter. Objective analysis reveals two dominant statistical modes of interannual variability of Red Sea SST: a whole-sea mode described by general warm or cool anomalies throughout the Red Sea (~60% of total variance), and a meridional gradient mode of opposing SST anomalies in the northern and southern Red Sea (~20% of total variance). The warm phase of the whole-sea mode corresponds to warm surface air temperature anomalies extending across the broader region and local surface wind anomalies opposite to the mean low-level circulation. The whole-sea mode is found to be a regional response to remote forcing by the East Atlantic/Western Russia (EAWR) pattern. The gradient mode, on the other hand, is a manifestation of superimposing (and statistically independent) remote impacts of El Niño-Southern Oscillation (ENSO) and the North Atlantic Oscillation (NAO) whereby ENSO drives SST anomalies in the southern Red Sea and the NAO drives SST anomalies in the northern Red Sea.

Plain Language Summary The Red Sea is climatically, ecologically, and economically important. The temperature at the surface of a body of water is a reliable indicator of its climatic and ecological conditions, and is readily observable from ships and Earth-orbiting satellites. Studying Red Sea temperature fluctuations from decades of such observations reveal what physical factors affect the temperature and currents within the Red Sea, both near and far. We found that the year-to-year fluctuations in Red Sea temperature are affected by three factors: (1) the air temperature of the Middle East region, (2) an arctic climate cycle called the North Atlantic Oscillation, and (3) a tropical climate cycle known as El Niño. These three factors cause temperature fluctuations in the Red Sea by affecting how much heat can be exchanged between the Red Sea and the atmosphere above. With this knowledge, it may be possible to predict Red Sea temperature fluctuations in advance, especially given that El Niño is predictable.

1. Introduction

The Red Sea is a major transportation highway for commercial shipping and its southern entrance, the strait of Bab-el-Mandeb, is considered one of the major global shipping choke points. In addition to shipping, artisanal fishing is significant within the Red Sea and important to the economies of adjoining countries. Scientifically, the Red Sea has been described as a thermohaline-driven, inverse estuarine circulation such that it provides a natural laboratory for studying the effects of ocean and climate physics with some relevance to the global scale thermohaline circulation or Atlantic Meridional Overturning Circulation (AMOC) by way of analogy (Sofianos & Johns, 2017). Because the Red Sea is a semienclosed basin, its boundaries constrain the physical processes so that its response to various types of forcing can be more easily examined than those of the AMOC. Although the Red Sea is influenced by water masses from the Indian Ocean (Sofianos & Johns, 2003, 2007), its semienclosed structure limits its direct influence from larger scale ocean phenomena compared to other marginal seas, leading to an hypothesis that much of its temporal variability will be driven by atmospheric forcing. Because of the potential

coupling of deep water formation with extreme cooling events, it is essential to learn what factors contribute to such anomalous atmospheric conditions, and to understanding how climate change may be shifting this exchange.

Considerable attention has been given to long-term trends, abrupt warmings, anthropogenic climate change and implications for coral reefs (Cantin et al., 2010; Felis et al., 2000). Recent work has identified both the seasonal and secular patterns of SST and wind variability in the Red Sea. There has been an overall secular trend of rising SST and slowing wind speed in the Red Sea as evidenced in data since the mid 1980s (Chaidez et al., 2017; Langodan et al., 2017; Nandkeolyar et al., 2013; Raitsos et al., 2011), while Eladawy et al. (2017) found insignificant SST and wind trends in the northern Red Sea using satellite data from 2000-2014. These works also identified an abrupt increase in Red Sea SST in the 1992–1994 time period, coincident with the warm period in the Pacific associated with the two successive El Niños during 1990–1994.

Felis et al. (2000) examined a 245 year long record of $\delta^{18}O$ from a coral core obtained at Ras Um Sid at the southern tip of the Sinai Peninsula. Correlating $\delta^{18}O$ fluctuations with SST and related salinity variations, it was concluded that the northern Red Sea was modulated by both the North Atlantic Oscillation (NAO) and El Niño-Southern Oscillation (ENSO)/North Pacific Ocean dynamics. Papadopoulos et al. (2013) argued that the sea level pressure gradient and the resulting wind stress have a strong effect on the surface heat fluxes. Abualnaja et al. (2015) examined the interaction between heat fluxes and several climate indicators. They found that heat fluxes in the northern Red Sea appeared to be modulated by the NAO, East Atlantic/Western Russia (EAWR) pattern and Indian Monsoon Index (IMI), especially during winter and that ENSO was most influential in the southern Red Sea (Abualnaja et al., 2015). Raitsos et al. (2015) and Dasari et al. (2017) examined the influence of ENSO on the low-level wind field in the Red Sea region with attention to the so-called Red Sea Convergence Zone (RSCZ) and Red Sea Trough (RST), showing that ENSO modulates the position of the RSCZ/RST system with an accompanying adjustment of the scale of the winds blowing along the major axis of the Red Sea.

Although several studies have found linkages between well-known modes of interannual climate variability and the Red Sea, a Red Sea-centric view investigating objectively the controls on SST at that time scale has not been presented. The present study aims to help bridge the gap between seasonal dynamics and longer-term variability, and to extend our recently growing knowledge of interannual variability of SST in the Red Sea by systematically describing the statistics and potential modes of variability at the interannual time scale toward understand their associated climate mechanisms including the influence of remote teleconnections. In the following section, potentially useful data sets are reviewed and compared, justifying the use of a particular data set for the purpose of this investigation. Results including examination of scales of variability, objective statistical analysis, and diagnosis of relationships with physical processes and large-scale climate phenomena are given in section 3. Finally, a brief summary of the major results and discussion of paths forward are given in section 4.

2. Data and Methods

Several widely used, satellite-derived, near-global gridded SST data sets exist that are potentially appropriate for investigating the spatiotemporal variability of SST in the Red Sea. Such data sets include but are not necessarily limited to the following.

1. NASA Moderate Resolution Imaging Spectroradiometer (MODIS; Kilpatrick et al., 2015) level 3 processed infrared SST data products are available at 4 and 9 km spatial resolution, from 2000 to present (on board the Terra satellite) and from 2002 to present (on board the Aqua satellite). Data are available for download at https://oceancolor.gsfc.nasa.gov/cgi/l3.
2. The NOAA Optimal Interpolation (OI) v2, high-resolution (Reynolds et al., 2007) SST data product is a blend of infrared satellite retrievals from the Advanced Very High Resolution Radiometer (AVHRR), which is independent of MODIS, and in situ measurements from the International Comprehensive Ocean Atmosphere Data Set (ICOADS; Worley et al., 2005). The NOAA OI v2 data are available at 0.25° spatial resolution (or 25–27 km × 28 km in the Red Sea), from 1982 to present. Data are available for download at https://www.esrl.noaa.gov/psd/data/gridded/data.noaa.oisst.v2.highres.html.
3. The NOAA AVHRR Pathfinder v5.3 (Casey et al., 2010) level 3C SST data product is strictly based on infrared retrievals from the AVHRR satellite and is available at 4 km spatial resolution, from 1982 to 2014. Data are

available for download at https://data.nodc.noaa.gov/cgi-bin/iso?id=gov.noaa.nodc:AVHRR_ Pathfinder-NCEI-L3C-v5.3.

4. Tropical Rainfall Measuring Mission (TRMM) Microwave Imager (TMI) v7.1 (Wentz et al., 2015a) and Global Precipitation Measurement (GPM) Microwave Imager (GMI) v8.1 (Wentz et al., 2015b) SST data products, processed by Remote Sensing Systems, are available at 0.25° spatial resolution. A complete temporal record could be constructed by merging TMI (1998–2014) and GMI (2014 to present). Data are available for download at http://www.remss.com/missions.

There are several tradeoffs among these data sets; chief among them, in the present context, is between record length and spatial resolution. The aim of the present study is to describe and understand the climatic context of the variability of SST at relatively broad spatial scales within the basin (i.e., much larger than individual eddies) and on relatively long and persistent temporal scales (i.e., the year-to-year variation of seasonal means). Thus, a longer record length should be prioritized for the benefit of statistics, but only so long as the spatial resolution is deemed sufficient to describe meaningful spatial patterns at monthly and longer time scales.

Given that the width (or minor axis) of the Red Sea varies between ~200 km (in the north, away from the Gulfs of Suez and Aqaba) and ~300 km (in the south, away from the Bab-el-Mandeb Strait), it is not unreasonable to propose that a spatial resolution of 0.25° may be sufficient for the above stated purpose. In addition to the longest continuous temporal record (35 complete calendar years), the NOAA OI v2 benefits from the input of in situ SST measurements (largely due to container ships, in the case of the Red Sea). Due to a consistently high volume of shipping traffic through the Red Sea, there is a remarkably high density of in situ measurements in the ICOADS data bank for the OI analysis procedure to draw from (Figure 1). In fact, over the period 1982–2016, the in situ sampling density in the Red Sea rivals that of many regions globally, with most 1° × 1° grid boxes running down the major axis of the Red Sea having an average of ~50 in situ SST observations per month.

A direct comparison of the spatiotemporal variability of SST in the Red Sea between the NOAA OI v2 and a higher-resolution data product (MODIS: Terra, daytime, 11 μm, 9 km) for the overlapping period (2001–2016) is encouraging (Figure 2). The overall spatial variation present in the annual mean is extremely consistent between the two data products, with the NOAA OI v2 warmer by ~0.5°C relative to MODIS in the southern half of the Red Sea. Aside from possible sensor and calibration differences between AVHRR and MODIS, the authors hypothesize that the warm southern bias may be partially related to seasonally dependent atmospheric corrections affecting MODIS, whereas NOAA OI v2 is constrained year-round by in situ measurements. Both data products reveal the surface thermal manifestations of the well-known and persistent large-scale cyclonic eddy-like circulation in the central-northern Red Sea (e.g., Sofianos & Johns, 2007; Yao et al., 2014a, 2014b), as evident in the northward (southward) tilt of isotherms on the eastern (western) half of the basin, as well as that of the seasonal intrusion of relatively cool, fresh, and nutrient-rich Gulf of Aden Intermediate Water (GAIW) into the far southern Red Sea through the Bab-el-Mandeb Strait (Churchill et al., 2014; Dreano et al., 2016; Sofianos & Johns, 2007; Wafar et al., 2016).

The temporal variability of SST is also extremely similar between the two data products (Figure 2, bottom row and Figure 3). For monthly SST averaged throughout the Red Sea, the correlation between NOAA OI v2

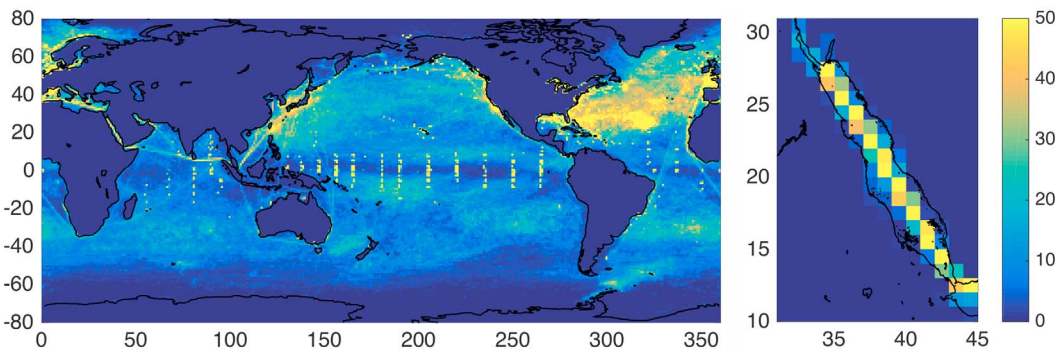

Figure 1. Average number of in situ SST observations per month per 1° × 1° grid box in the ICOADS data bank from 1982 to 2016. The color bar shown on the right applies to both plots.

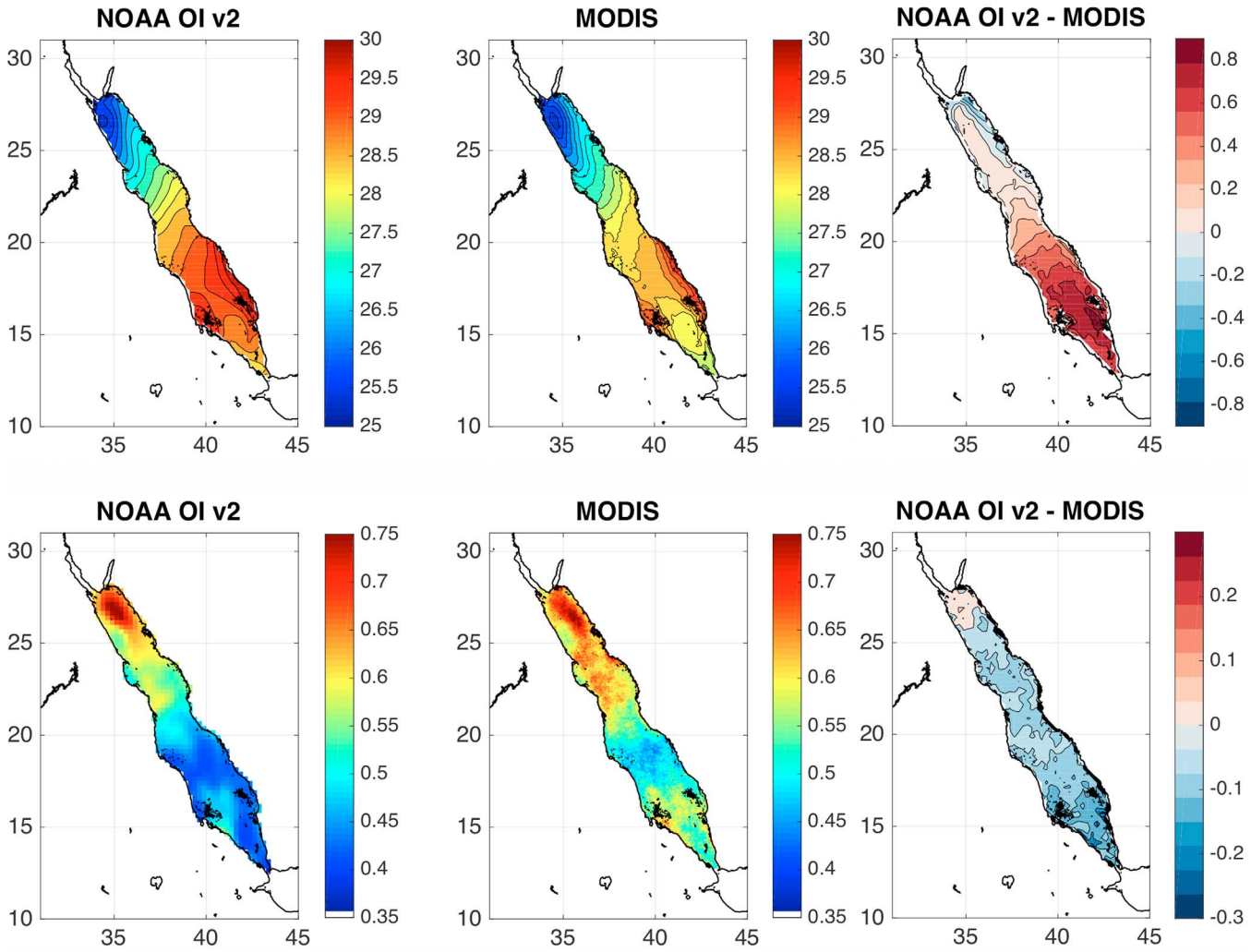

Figure 2. Comparison of time-averaged (2001–2016) SST (°C) from the 0.25°–resolution NOAA OI v2 product and the 9 km resolution Terra MODIS 11 μm daytime product (top row). Bottom row: as in top row, but for the standard deviation (°C) of monthly SST anomalies. Difference maps in the right column were produced by regridding (via linear interpolation) the MODIS fields to the 0.25° resolution grid of the NOAA OI v2 product.

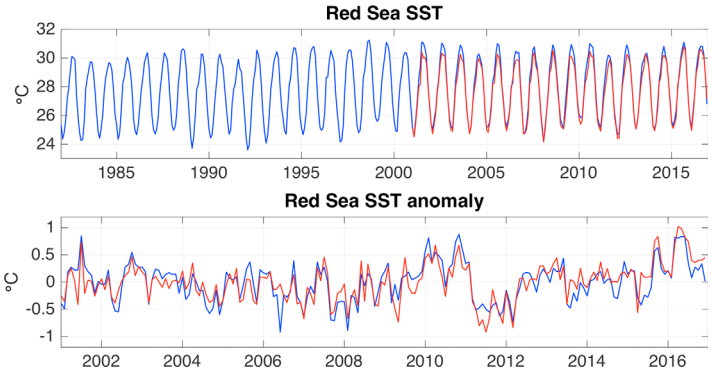

Figure 3. Comparison of Red Sea-averaged monthly SST (top) and SST anomalies (bottom) between the 0.25° resolution NOAA OI v2 product (blue lines) and the 9 km resolution Terra MODIS 11 μm daytime product (red lines). Monthly anomalies shown in the bottom plot were computed relative to the same base climatology (2001–2016). Note that the top and bottom plots have different *x* axis scales (the bottom only covers the overlapping time period).

and MODIS is 0.99 (including the seasonal cycle) or 0.83 for anomalies (i.e., after removing the mean seasonal cycle). By visual inspection (Figure 3, bottom plot), the high correlation appears to be the result of close correspondence on a broad range of temporal scales from sharp intraseasonal anomalies to more subtle secular trends. Splitting the basin into the northern and southern Red Sea at 20°N as well as the gradient between the two (Figure 4) also reveals impressive temporal agreement, with anomaly correlations of 0.86, 0.76, and 0.83, respectively. To summarize, in terms of the spatial patterns of the mean climatology as well as the intraseasonal-to-decadal variations about the climatology, the 0.25° NOAA OI v2 and 9 km MODIS products are nearly indistinguishable. For that reason and other considerations discussed above, the detailed analysis of interannual variability of SST in the Red Sea presented hereafter is based on the NOAA OI v2 data set.

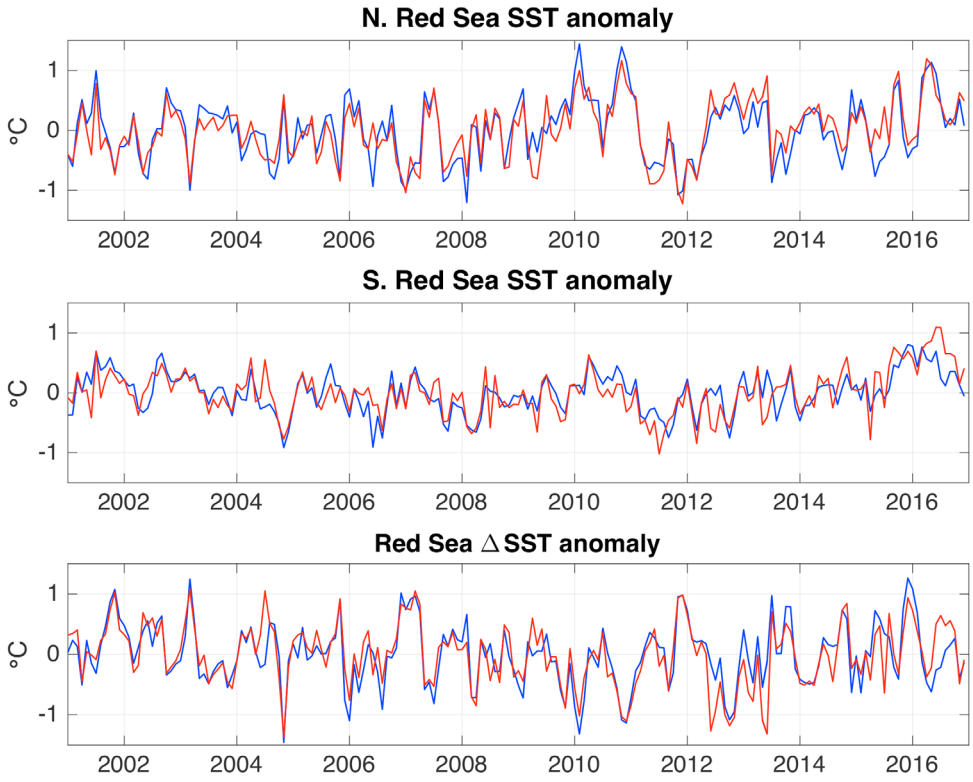

Figure 4. As in Figure 3 (bottom) but for monthly SST anomalies averaged over the (top) northern (>20°N) Red Sea, (middle) southern (<20°N) Red Sea, and (bottom) the meridional SST gradient using 20°N as the boundary between the northern and southern Red Sea.

Ancillary observational data sets employed in the present study include monthly global 10 m wind and 2 m air temperature fields from the NCEP/DOE Atmospheric Reanalysis II ("NCEP2") (Kanamitsu et al., 2002), monthly El Niño-Southern Oscillation (ENSO), North Atlantic Oscillation (NAO), and East Atlantic/Western Russia (EAWR) indices from the NOAA Climate Prediction Center (see Acknowledgments), and high-resolution coastlines from the Global Self-consistent, Hierarchical, High-resolution Geography (GSHHG) database version 2.2.3 (Wessel & Smith, 1996).

3. Results

3.1. Spatial and Temporal Scales of SST Variability

The observed annual mean SST in the Red Sea, averaged over 1982–2016, varies from ~25°C in the extreme northwest corner to ~29°C along the southern Saudi coast (a distance of ~1,000 km) (Figure 5a). The spatial patterns during boreal summer (June–August) and winter (December–February) differ substantially in response to seasonally varying solar forcing and surface wind as shown through heat fluxes by Abualnaja et al. (2015) and Papadopoulos et al. (2013). The mean boreal summer SST field exhibits SST varying from 27.5°C in the northwest to >31°C in the extreme south (Figure 5b), while the mean winter SST pattern is qualitatively very similar to the annual mean but with SSTs cooler by 1–2°C (Figure 5c).

The highest amplitude temporal variability of SST (after removing the mean seasonal cycle) is found in the northern half of the Red Sea during boreal winter (Figures 5d–5f). The standard deviation of monthly SST anomalies ranges from ~0.5°C in the southern Red Sea to >0.7°C in the northern Red Sea. This gradient of variability is enhanced for the wintertime seasonal means (ranging from 0.3°C to 0.6°C), whereas there is relatively small interannual variability of summertime SST throughout the Red Sea (0.3–0.4°C). The latter is likely due to the strong summertime stratification in the Red Sea capping the variability within the upper 50–100 m, whereas winter SST is a function of air temperature and thus heat losses via latent and sensible heat fluxes as well as the amount and depth of mixing (Papadopoulos et al., 2015; Yao et al., 2014a, 2014b).

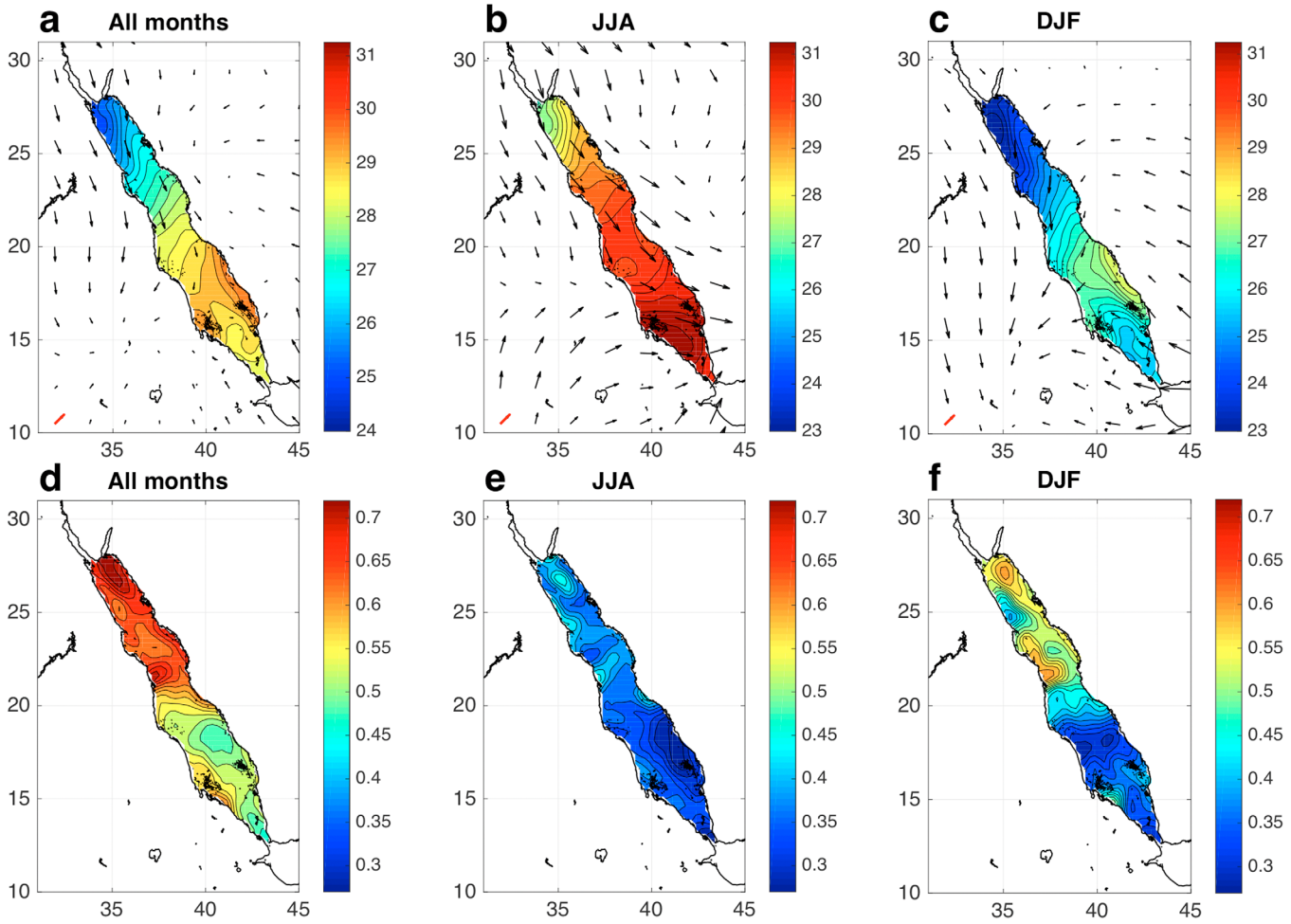

Figure 5. (a–c) Time-averaged (1982–2016) SST (°C) from the 0.25° resolution NOAA OI v2 product and 10 m wind from the NCEP2 reanalysis (a, d) over all months, (b, e) boreal summer, and (c, f) boreal winter. A scale vector of (2,2) m/s is provided in the lower-left corner (colored red to aid identification). (d–f) Bottom row: as in (a–c) top row, but for the standard deviation (°C) of detrended (d) monthly and (e, f) seasonal SST anomalies.

In comparison with SST variability globally, these anomalies are relatively modest. In the extratropical North Pacific, the northwestern Atlantic (Gulf Stream region) and the eastern equatorial Pacific, the standard deviation of monthly SST anomalies (not shown) reaches approximately twice the amplitude as that of the northern Red Sea.

Given that the observed gradients of mean SST and amplitude of SST interannual variability, the latter of which are particularly sharp, are primarily oriented along the major axis of the Red Sea ("meridional" hereafter), it makes sense to examine the temporal variability in the northern and southern Red Sea separately and in contrast to one another. Using 20°N as a general boundary between the two regional domains of the Red Sea, the detrended monthly and interannual variability of area-averaged SST indices along with the meridional gradient thereof are shown in Figure 6, with their spectral content displayed in Figures 7 and 8. The strong observed interannual variability of wintertime SST in the northern Red Sea is statistically robust at periods between 3 and 5 years (Figure 8, top right), which appears to translate into the strongest and most significant spectral peak in the wintertime meridional SST gradient at ~5 years (Figure 7, top right). The importance of the robustness of variability at this time scale and in this spatial configuration will be clear in section 3.3 below focusing on remote forcing of wintertime SST across the Red Sea.

The spatial domains for the above SST indices were defined approximately based on emergent patterns in the mean climatology and amplitudes of variability about that climatology. Composite analysis recovers the actual observed SST anomaly patterns corresponding to those box indices with some regional detail

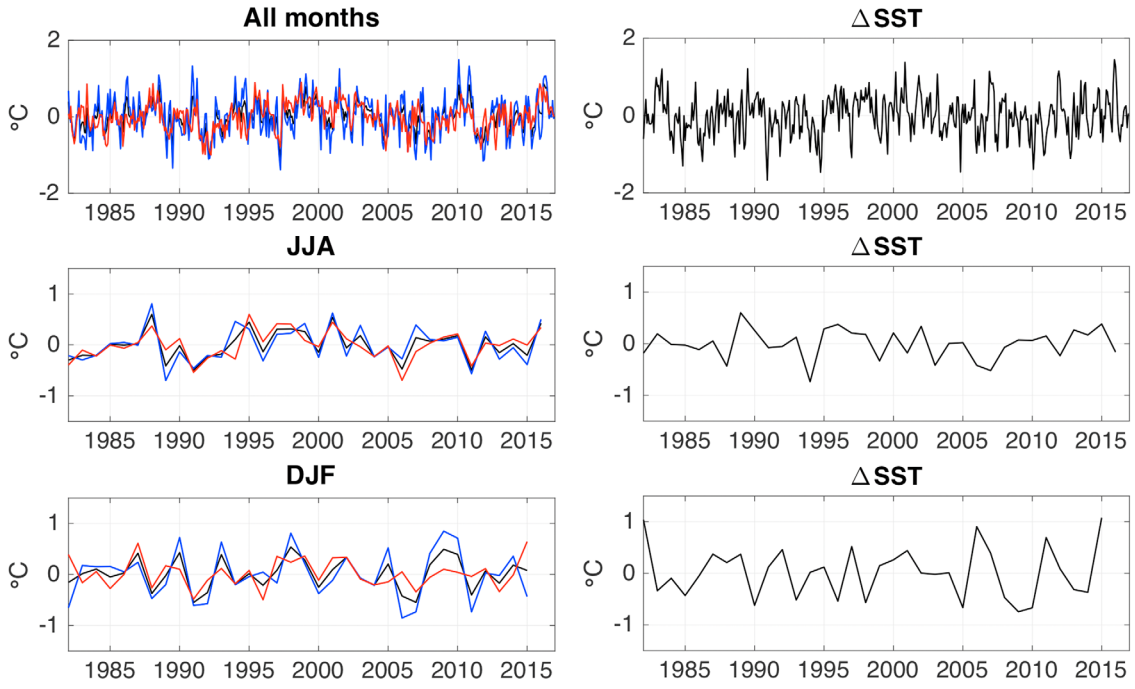

Figure 6. Time series of detrended SST (°C) averaged over the Red Sea (black), northern (>20°N) Red Sea (blue), southern (<20°N) Red Sea (red), and the meridional SST gradient (°C) using 20°N as the boundary between the northern and southern Red Sea (black, right column) for (top row) monthly anomalies, (middle row) boreal summer, and (bottom row) boreal winter.

(Figure 9). When the monthly SST anomaly averaged across the entire Red Sea is positive, statistically significant positive SST anomalies are found throughout the entire Red Sea, meaning that every grid point in the domain contributes to the anomalous warmth, but with greater anomalies (reaching 1°C in the composite difference) hugging the northern Saudi coast (≥20°N). The spatial pattern is similar when the

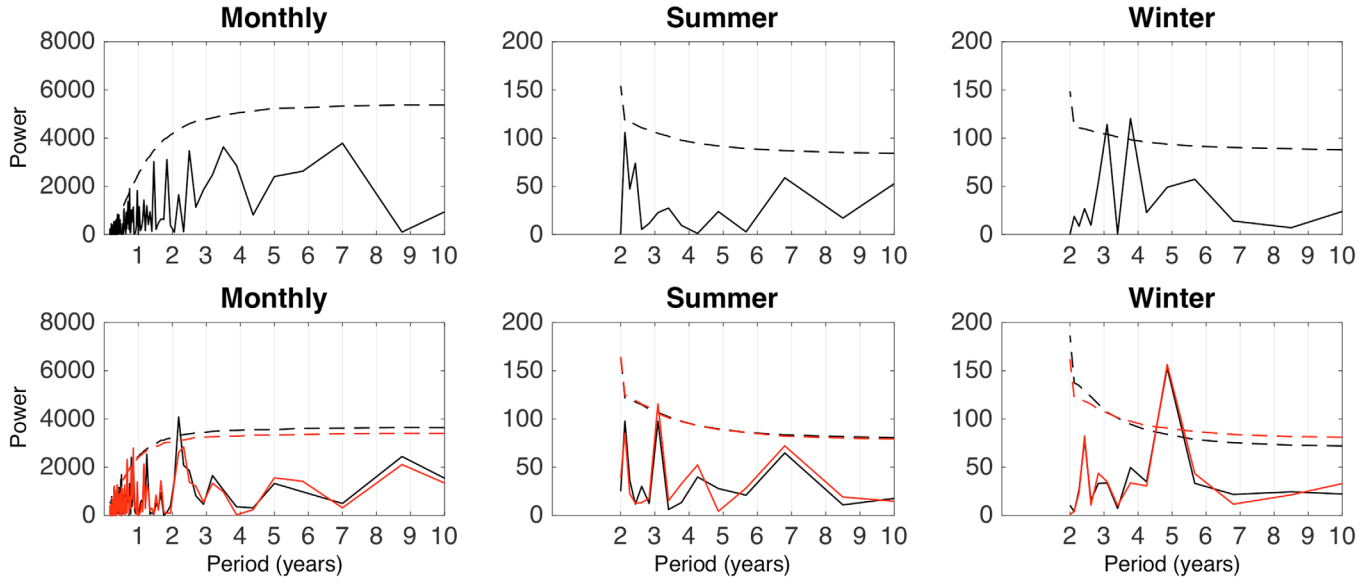

Figure 7. (top) Power spectra of Red Sea-averaged SST and (bottom) the meridional SST gradient within the Red Sea based on monthly anomalies, boreal summer (JJA) and boreal winter (DJF) seasonal means. Black lines in the bottom row indicate spectra of the meridional SST gradient using 20°N as the boundary between the northern and southern Red Sea, whereas red lines indicate spectra of the meridional SST gradient contrasting the extreme northern (>27°N) with the extreme southern (<15°N) Red Sea. Dashed lines indicate the 95% significance threshold relative to 100,000 Monte Carlo simulations using a first-order autoregressive model (i.e., red noise).

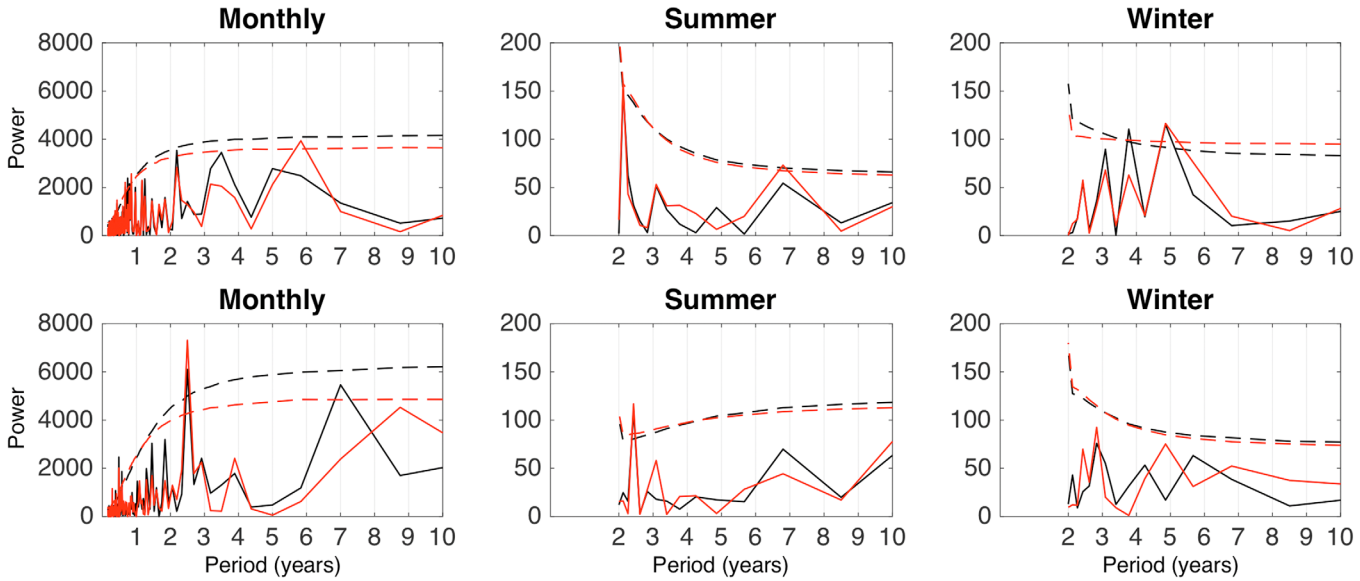

Figure 8. Power spectra of SST in the (top) northern and (bottom) southern Red Sea based on monthly anomalies, boreal summer (JJA) and boreal winter (DJF) seasonal means. Black lines indicate the spectra of SST indices averaged everywhere north or south of 20°N, whereas red lines indicate the spectra of SST indices averaged over the extreme northern (>27°N) or southern (<15°N) Red Sea. Dashed lines indicate the 95% significance threshold relative to 100,000 Monte Carlo simulations using a first-order autoregressive model (i.e., red noise).

SST anomaly fields are composited onto the northern Red Sea index, but with slightly greater anomalies along the northern Saudi coast and insignificant anomalies in the southern (<17°N) Red Sea. When the southern Red Sea is anomalously warm, there are on average ~0.8°C warmer SST anomalies relative to the cold phase of that index, with the warm anomalies spreading northward all the way to the Gulfs—again, exhibiting a zonal asymmetry such that warmer anomalies are observed along the eastern half of the basin, consistent with a northward transport via an eastern boundary current (e.g., Bower & Farrar, 2015; Sofianos & Johns, 2002, 2003). Finally, compositing the SST anomaly fields onto the index defined by the meridional SST gradient between the northern and southern Red Sea reveals an out-of-phase relationship between the northern and extreme southern Red Sea wherein the mean meridional SST gradient along the major axis is strengthened by up to 1.5°C.

The time series and composite analyses shown here begin to highlight a tendency for the northern and southern Red Sea to vary together, but with a significant component of the total variability in each half of the basin occurring independent of—or even out of phase with—the other. Such potential modes of spatio-temporal variability are explored in a more objective statistical framework in the following section.

3.2. Objective Analysis

In this section, empirical orthogonal function (EOF) analysis (also known as principle component (PC) analysis) is applied to monthly and seasonal SST anomaly fields from 1982 to 2016 using the same spatial domain of the Red Sea (i.e., where data appear on all previous map figures), with the exception of the Gulf of Aden. An excellent review of the EOF methodology, including the mathematics and practical implementation, is given by Björnsson and Venegas (1996). The essence of EOF analysis is to objectively reduce the space of a data set to its most dominant time-varying patterns of variability (referred to as modes), with the important caveat that each mode be spatially and temporally orthogonal to the others. As is common practice and consistent with the scope of the present study, the SST fields were first detrended in order for the EOF analysis to capture the underlying modes of interannual variability.

Regardless of whether the EOF analysis procedure is applied to monthly anomalies or seasonal fields (boreal summer and winter separately), two dominant modes emerge. For the time being, we will only refer to these as "statistical" modes, rather than true "dynamical" modes such as those that tend to occur through coupling with the atmosphere in large, tropical ocean basins (e.g., ENSO or Indian Ocean Dipole (IOD)). The first two modes explain ~80% of the total variance of the data (Figure 10), with the exact contributions of

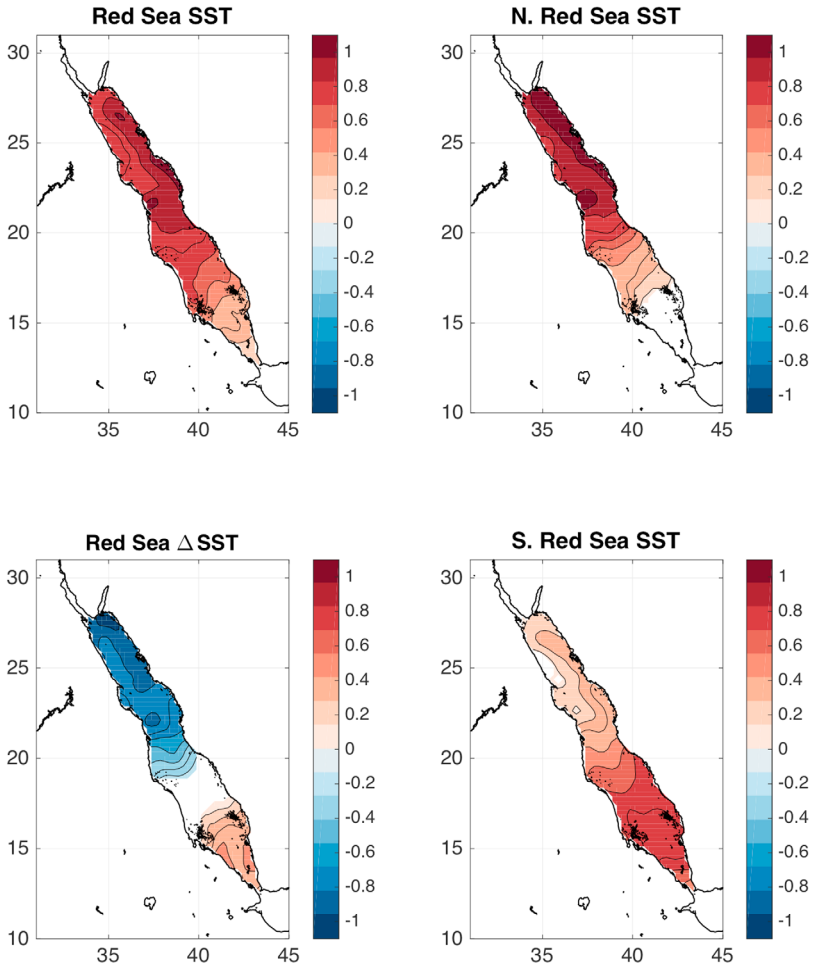

Figure 9. Difference of monthly SST anomaly (°C) composited on the four indices shown in the top row of Figure 6: Red Sea SST (top left), the meridional SST gradient using 20°N as the boundary (bottom left) between the northern and southern Red Sea, (top right) northern (>20°) Red Sea, and (bottom right) southern (<20°) Red Sea. The threshold for inclusion in the composite means was exceeding a value of ±0.1°C. Only values significant at the 95% confidence level are shown (difference exceeding ±2 standard errors). Composite difference results for boreal summer and boreal winter are qualitative very similar, with boreal winter having greater amplitudes than boreal summer (not shown).

the first and second modes to the total varying slightly between season (but generally a 60–20% split). The higher-order modes explain no more than a few percent of the total variance and will not be discussed further.

The spatial patterns and temporal characteristics of the two leading modes are similar between the monthly and seasonal anomaly fields, but with some interesting differences. The two leading modes identified in the monthly SST anomalies (Figure 11), for example, include what one might refer to as a "whole-sea" mode (EOF1) wherein the entire Red Sea is varying between anomalously warm everywhere and anomalously cool everywhere, and a "gradient" mode (EOF2) wherein SST anomalies are varying out of phase with ~20°N serving as the boundary between the two. Little asymmetry is manifest within the gradient mode, whereas the whole-sea mode exhibits strong meridional and zonal asymmetries akin to the composite analysis (Figure 9). Those asymmetries include the eastern half of the northern Red Sea exhibiting stronger variability, and the extreme southern Red Sea exhibiting weaker variability compared to the central and north. To confirm the dominance of the two leading modes, as well as their near-equivalence to the aforementioned indices based on simple area averages, the area-averaged Red Sea SST and meridional SST gradient indices are plotted on top of PC1 (whole-sea mode) and PC2 (gradient mode); their correlations with the PCs are 0.98 and 0.84, respectively. Although beyond the scope of the present study, there is also

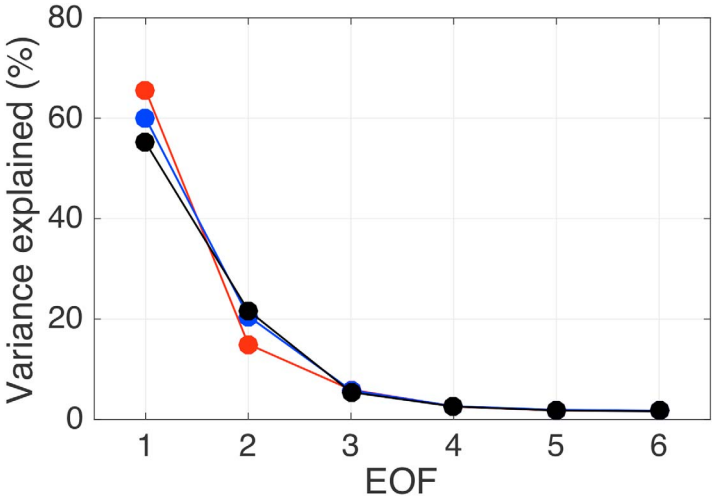

Figure 10. Percent of the total variance explained by each of the leading six EOFs of monthly SST anomalies (black), boreal summer SST (red), and boreal winter SST (blue).

potentially interesting and robust decadal-scale variability in both of the leading modes of SST variability in the Red Sea.

There are a few interesting differences between the results of the EOF analysis applied to boreal summer and winter SST fields (Figures 12 and 13). The summertime whole-sea mode is more homogeneous or free of asymmetries; the wintertime whole-sea mode, in addition to being higher amplitude, actually exhibits slightly negative SST anomalies in the extreme southern Red Sea and thus projects very slightly onto a physical gradient depending on how it is defined. The gradient mode also explains 6% more of the total variability in winter than in summer. In other words, wintertime SST variability in the Red Sea has a very strong preference for there to be a meridional gradient in the expression of the overall anomaly field. The regional climatic context and remote forcing for the variability highlighted by objective analysis is explored further in the following section.

3.3. Regional and Remote Forcing Mechanisms

To first provide the regional climatic context associated with the leading modes of SST variability identified objectively above, and explore their possible physical mechanisms, simple linear regression is conducted between the PC1 and PC2 time series and surface climate fields (2 m air temperature [T_{2m}] and 10 m zonal and meridional wind) from the NCEP2 reanalysis (Kanamitsu et al., 2002). Based on the monthly anomalies (Figure 14), it is immediately clear that the positive phase of the whole-sea mode is associated with warm surface air temperatures spread across the entire middle eastern region including northeastern

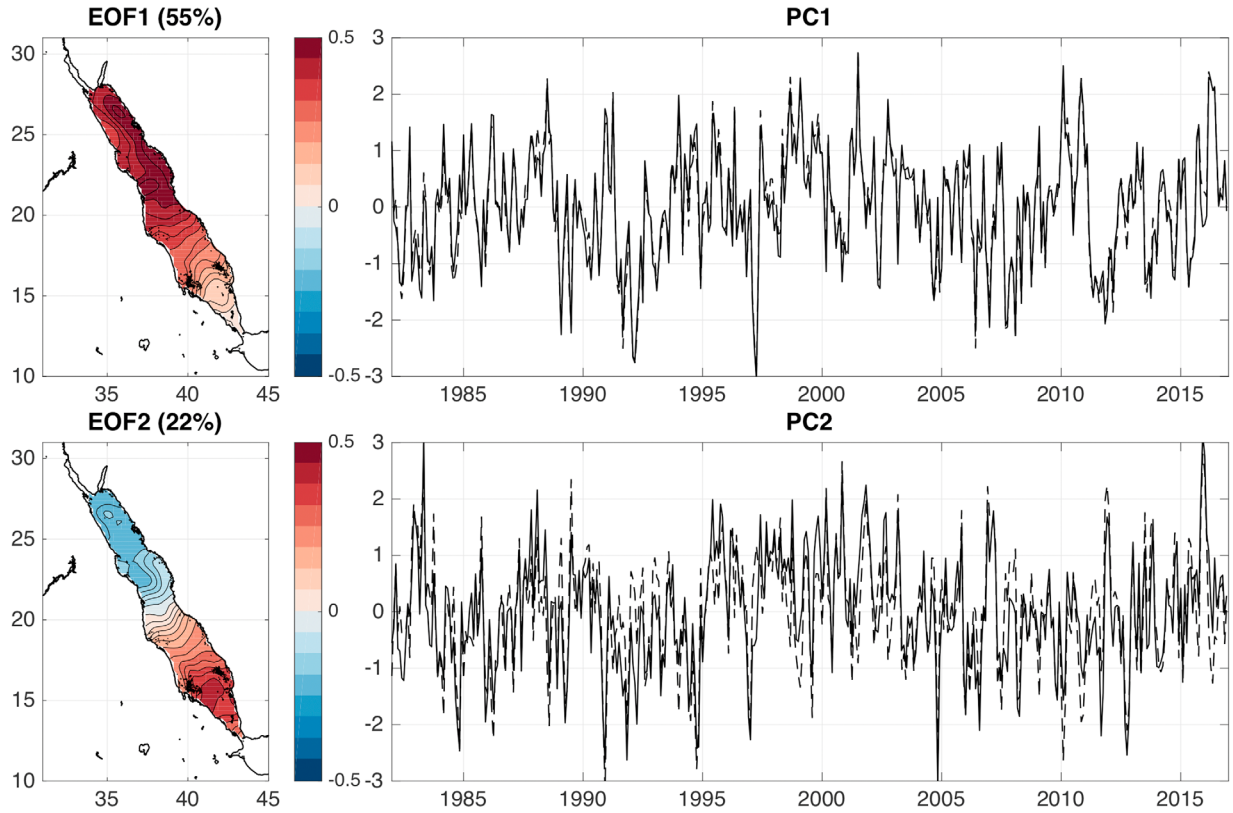

Figure 11. Leading two EOFs (°C per standard deviation) and PCs (standard deviations) of monthly SST anomalies. The dashed line in the PC1 plot indicates the Red Sea-averaged SST, and the dashed line in the PC2 plot indicates the meridional SST gradient within the Red Sea using 20°N as the boundary between the northern and southern Red Sea.

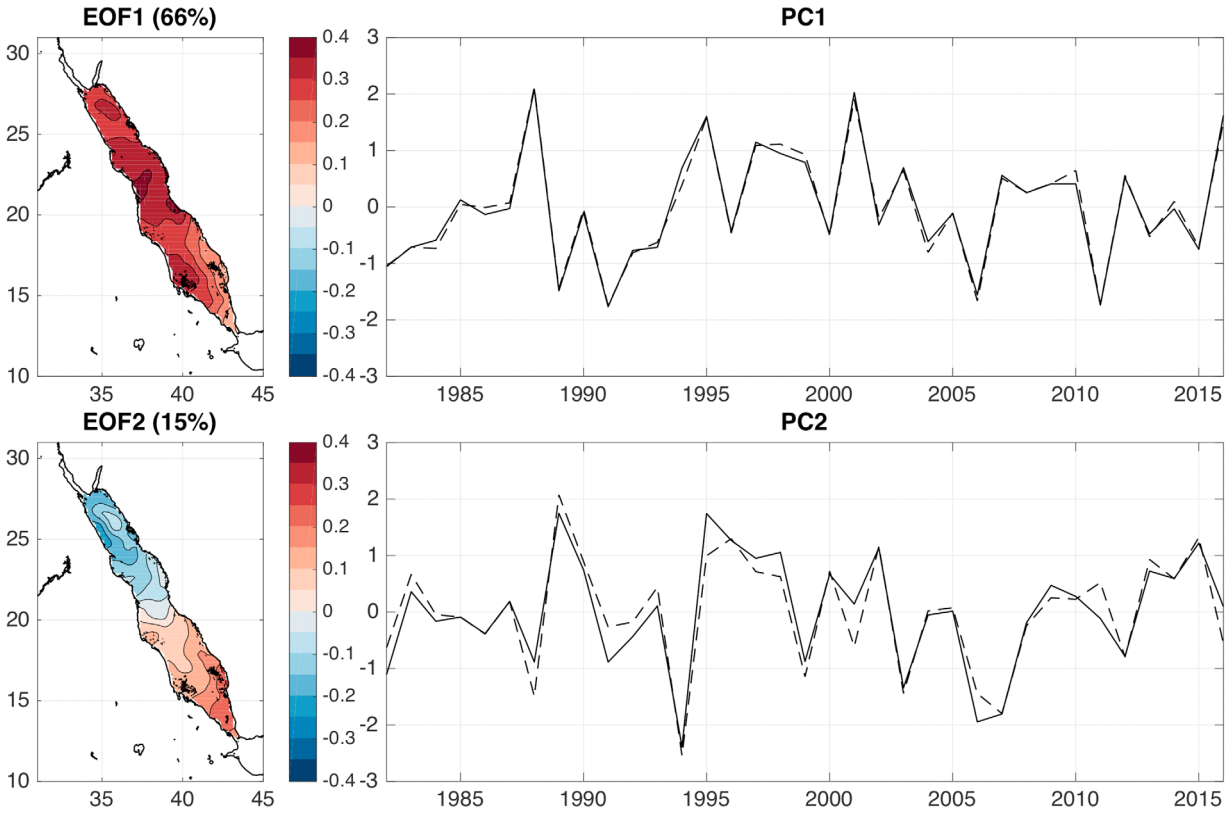

Figure 12. Leading two EOFs (°C per standard deviation) and PCs (standard deviations) of boreal summer SST anomalies. The dashed line in the PC1 plot indicates the Red Sea-averaged SST, and the dashed line in the PC2 plot indicates the meridional SST gradient within the Red Sea using 20°N as the boundary between the northern and southern Red Sea.

Africa, the eastern Mediterranean Sea, Turkey, and the Arabian Peninsula, and local surface wind anomalies opposite to the mean low-level circulation; hence, a reduction in the surface wind stress. This suggests that the whole-sea mode is a manifestation of broader regional climate variation and likely operates directly through surface turbulent heat fluxes. This analysis cannot distinguish between the role of wind-speed modulation of surface fluxes from air-temperature modulation of surface fluxes; sensitivity experiments with a regional ocean general circulation model (OGCM) are likely to resolve this question.

The positive phase of the so-called gradient mode also appears to be associated with broader regional climate variation in terms of surface air temperature forcing, with cool (warm) air temperature anomalies spreading from neighboring landmasses and water bodies across the northern (southern) Red Sea, while the associated surface wind forcing appears to be locally confined to the northern and central Red Sea. In the northern Red Sea, the enhancement of the mean wind would lead to cooler SST by enhancing evaporative fluxes and mixing, as well as driving anomalous upwelling in the extreme north. In the southern Red Sea, the warm SST anomalies appear to be associated with warm surface air temperature anomalies funneling into the Red Sea from the Indian Ocean via the Gulf of Aden, and potentially reduced northward advection of warm SST due to the southward wind over the central and northern Red Sea.

Separating the above diagnostic analysis into the boreal seasons illustrates that the regional anomalies are largely insignificant during summer (Figure 15) and highly significant during winter (Figure 16). However, the complexity of the wintertime modes prevents the simple PC-based regression technique from achieving such a clean separation. Hence, the regression of surface climate fields onto the SST gradient index based on area averages is also shown as a third plot in Figure 16. The patterns of regional-scale anomalous T_{2m} and 10 m winds is similar to that for the monthly anomalies without regard to season, but substantially stronger, and the implied physical mechanisms are therefore the same as those noted above.

The broader region surrounding the Red Sea has long been known to be directly impacted by the North Atlantic Oscillation (Visbeck et al., 2001) and the East Atlantic/Western Russia (EAWR) pattern (Barnston &

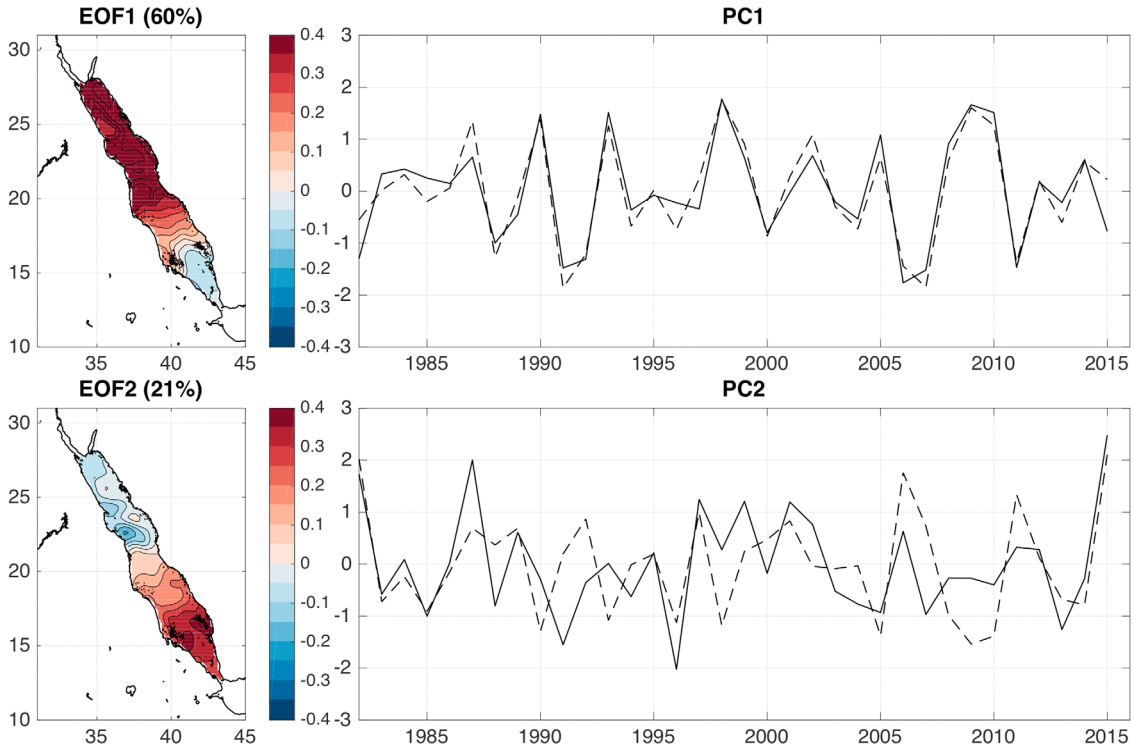

Figure 13. Leading two EOFs (°C per standard deviation) and PCs (standard deviations) of boreal winter SST anomalies. The dashed line in the PC1 plot indicates the Red Sea-averaged SST, and the dashed line in the PC2 plot indicates the meridional SST gradient within the Red Sea using 20°N as the boundary between the northern and southern Red Sea.

Livezey, 1987), while ENSO is known to indirectly influence the neighboring tropical Indian Ocean by way of atmospheric teleconnections (Bjerknes, 1969). The manifestations of these relationships within the Red Sea itself are easily detected by correlation and regression analysis between the Red Sea SST fields and established indices for the aforementioned three climate patterns (Figure 17). ENSO significantly modulates

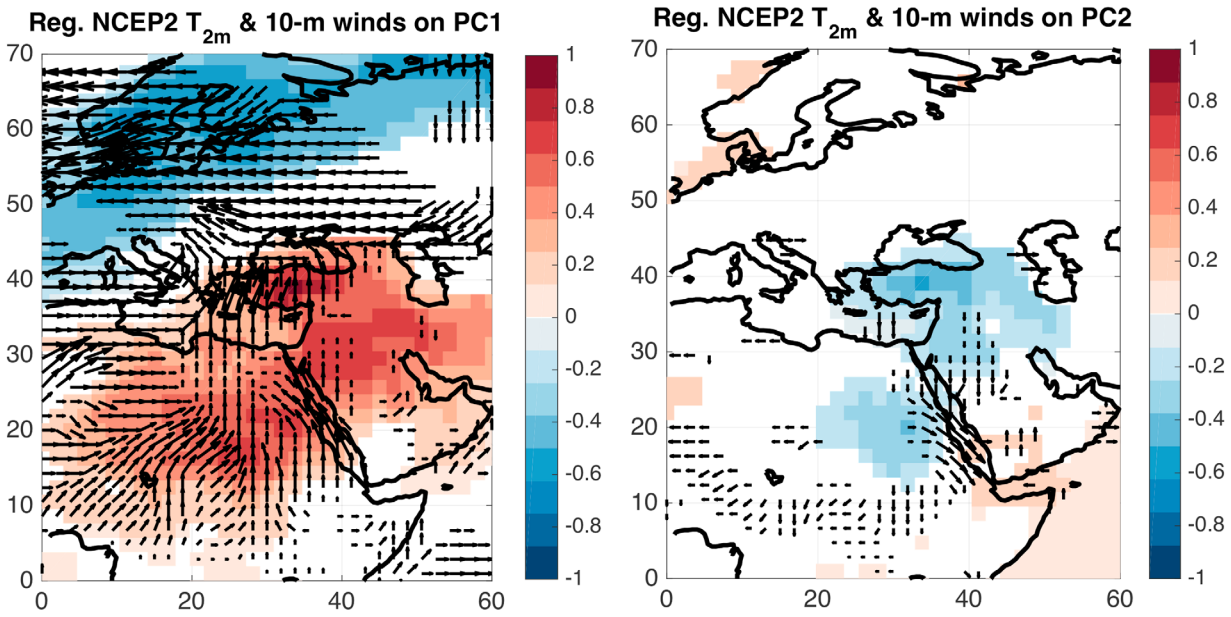

Figure 14. Monthly 2 m surface air temperature (°C) and 10 m wind anomalies from the NCEP2 reanalysis regressed onto (left) PC1 and (right) PC2 of monthly SST anomalies. Only values significant at the 99% confidence level are shown.

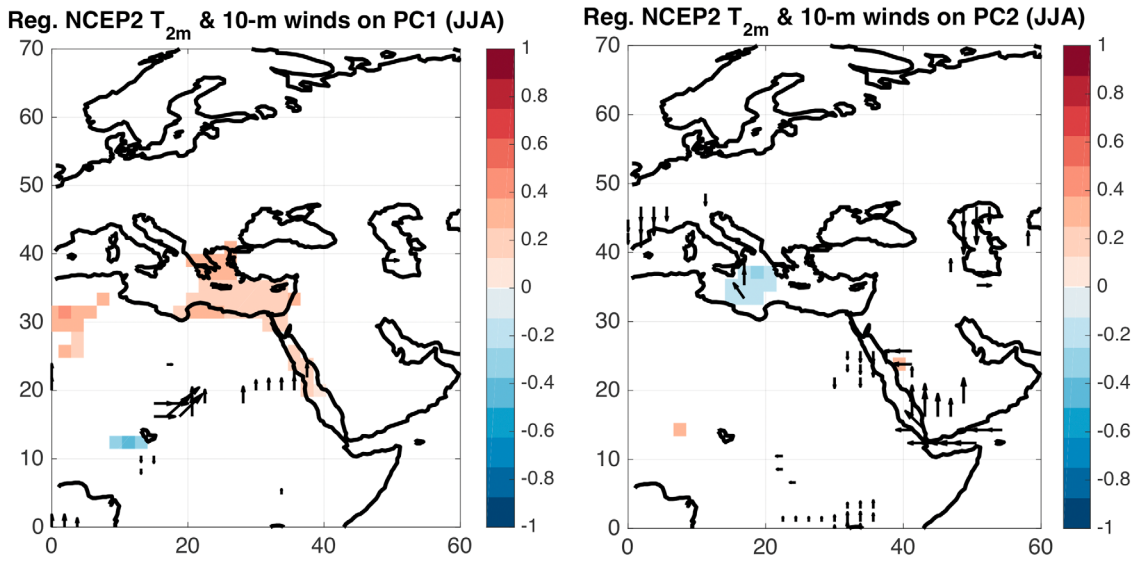

Figure 15. Boreal summer 2 m surface air temperature (°C) and 10 m wind from the NCEP2 reanalysis regressed onto (left) PC1 and (right) PC2 of boreal summer SST. Only values significant at the 99% confidence level are shown.

wintertime SST in the southern Red Sea (south of 18°N), with an amplitude of ~0.25°C during El Niño, and with a very modest response of the opposite sign in the central Red Sea (~22–24°N). In contrast, the NAO significantly modulates wintertime SST in the northern Red Sea (north of 22°N), with a similar amplitude as the ENSO impact observed in the southern Red Sea. Additionally, the EAWR pattern significantly impacts wintertime SST in a broad stretch of the eastern Red Sea from ~19°N to the northern end. The EAWR impact appears to be the most substantial in terms of both fraction of the Red Sea over which the phenomenon is significantly correlated with SST and the amplitude of SST response (>0.25°C). It should be noted that the boreal wintertime ENSO and NAO indices are perfectly uncorrelated ($r = 0.03$), and there were no significant correlations found between SST and either the NAO or ENSO for boreal summer, including with the preceding and subsequent wintertime NAO and ENSO indices (not shown). Despite the wintertime ENSO and EAWR indices being modestly correlated ($r = 0.4$), the SST response patterns are markedly different, suggesting the likelihood of independent mechanisms for remote forcing of SST anomalies.

The physical mechanisms by which ENSO, the NAO, and EAWR influence different areas of the Red Sea are identifiable by regressing T_{2m} onto said climate indices at the global scale (Figure 18). During an El Niño event, the entire tropical Indian Ocean is anomalously warm, with a prominent appendage of the overlying warm surface air temperature anomaly extending over the southern Arabian Peninsula, Horn of Africa, the

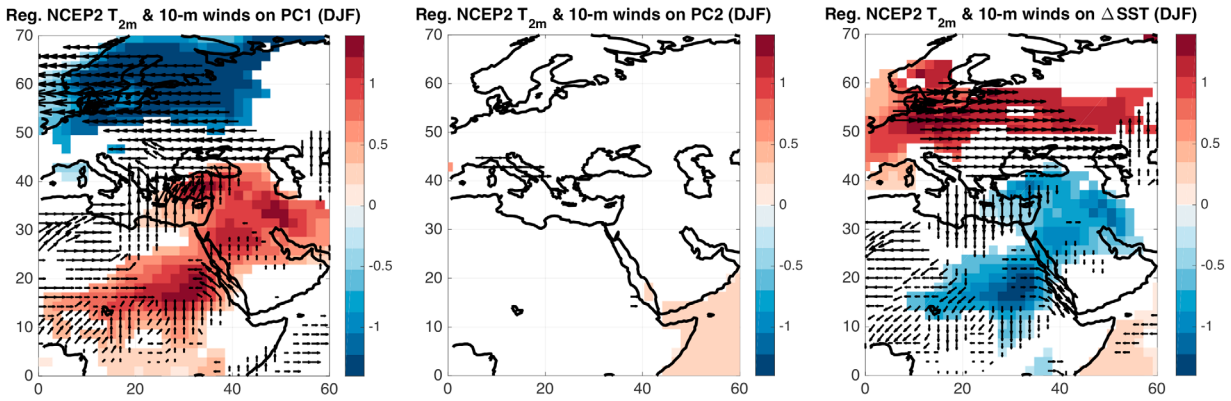

Figure 16. Boreal winter 2 m surface air temperature (°C) and 10 m wind from the NCEP2 reanalysis regressed onto (left) PC1 and (center) PC2 of boreal winter SST and onto the boreal winter meridional SST gradient using 20°N as the boundary between the northern and southern Red Sea (right). Only values significant at the 99% confidence level are shown.

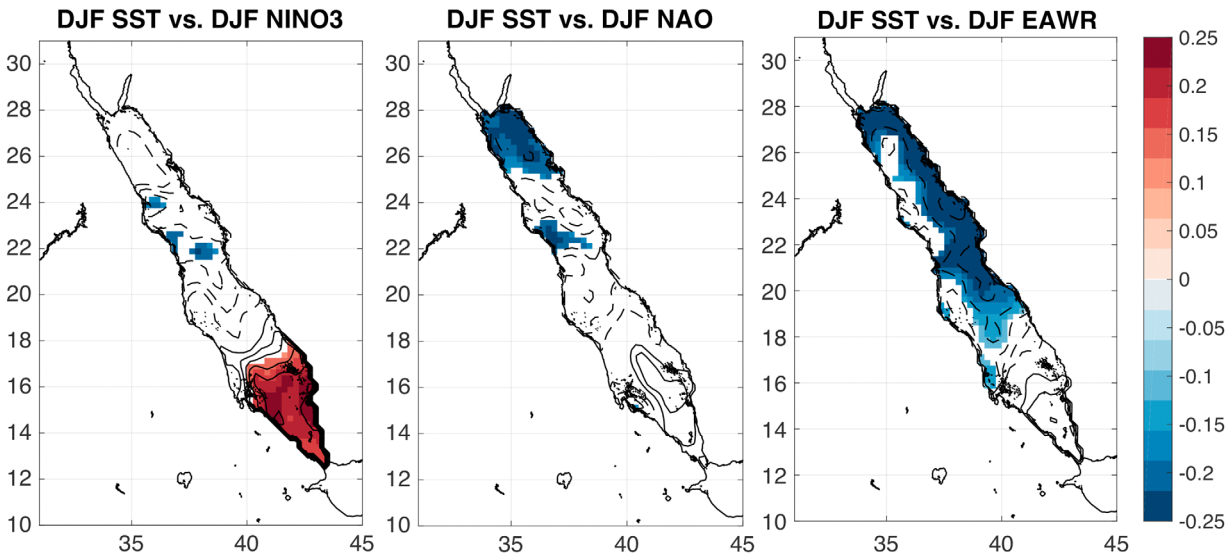

Figure 17. Boreal winter SST regressed onto (°C) (color shading) and correlated with (black contours) (left) the boreal winter NINO3 index, (center) the boreal winter NAO index, and (right) the boreal winter EAWR index. Only regression values significant at the 95% confidence level are shown. Correlation coefficients are contoured every 0.1 with the zero contour omitted.

Gulf of Aden in between and, finally, into the extreme southern Red Sea (Figure 18, top). Additionally, a cool T_{2m} anomaly persists centered over Egypt and onto the central Red Sea. Similarly, and as was illustrated vividly by Visbeck et al. (2001), the hemispheric-scale circulation anomaly comprising the NAO results in a very broad, negative T_{2m} anomaly extending from the western tropical Atlantic through northern Africa, the Mediterranean, and well past the Middle East, which coincidentally clips the northern Red Sea (Figure 18, bottom). The mechanism for the EAWR influencing wintertime Red Sea SST appears to be strictly one of surface heat flux (rather than dynamical forcing of the circulation by wind stress), as the EAWR features a prominent surface air temperature anomaly over the region of the Red Sea (spanning East Africa to northern Saudi Arabia) and the local surface wind response is insignificant (Figure 19).

Both ENSO and the NAO have very large-scale footprints, and it is merely the accident of geography that these two statistically independent modes of internal climate variability impact opposite ends of the Red Sea during the same season. It would thus seem logical that the combined effect of ENSO and NAO is to generate interannual SST variability projecting onto the whole-sea mode (in the case of, e.g., El Niño and negative NAO) and the meridional gradient mode of wintertime SST (in the case of, e.g., El Niño and positive NAO). This indeed appears to be the case, and the forcing mechanism is not necessarily restricted to large-scale circulation anomalies remotely modulating the regional surface air temperature field. For example, linearly superimposing the regional 10 m wind anomalies associated with positive phases of ENSO and NAO (as one can do by eye, based on the first two plots of Figure 19) results in local wind forcing that is virtually indistinguishable from that associated with the negative phase of the whole-sea mode and/or the positive phase of the gradient mode (Figure 16, left and right plots). The surface wind anomalies in the southern Red Sea associated with El Niño are counter to the mean local wind field, and thus serve to reduce surface heat fluxes and warm SST. This result is quite the opposite of that found by Dasari et al. (2017), who found an increase in the southeasterly wind over the southern Red Sea for a composite El Niño event. However, there are a number of important differences in the methods and data sets used, particularly a focus on a different season as the present analysis. In contrast, the surface wind anomalies in the northern Red Sea associated with positive NAO are aligned with the mean local wind field, and thus serve to enhance evaporative heat loss and cool SST. Overall, the dominance of the EAWR in the wintertime Red Sea variability is evident in the fact that the EAWR index is significantly (99%) correlated ($r = 0.5$) with the first PC of wintertime SST, which is consistent with the leading EOF pattern (the so-called whole-sea mode) having a relatively stronger loading in the same area as the regression map of wintertime SST on the EAWR index including significant values.

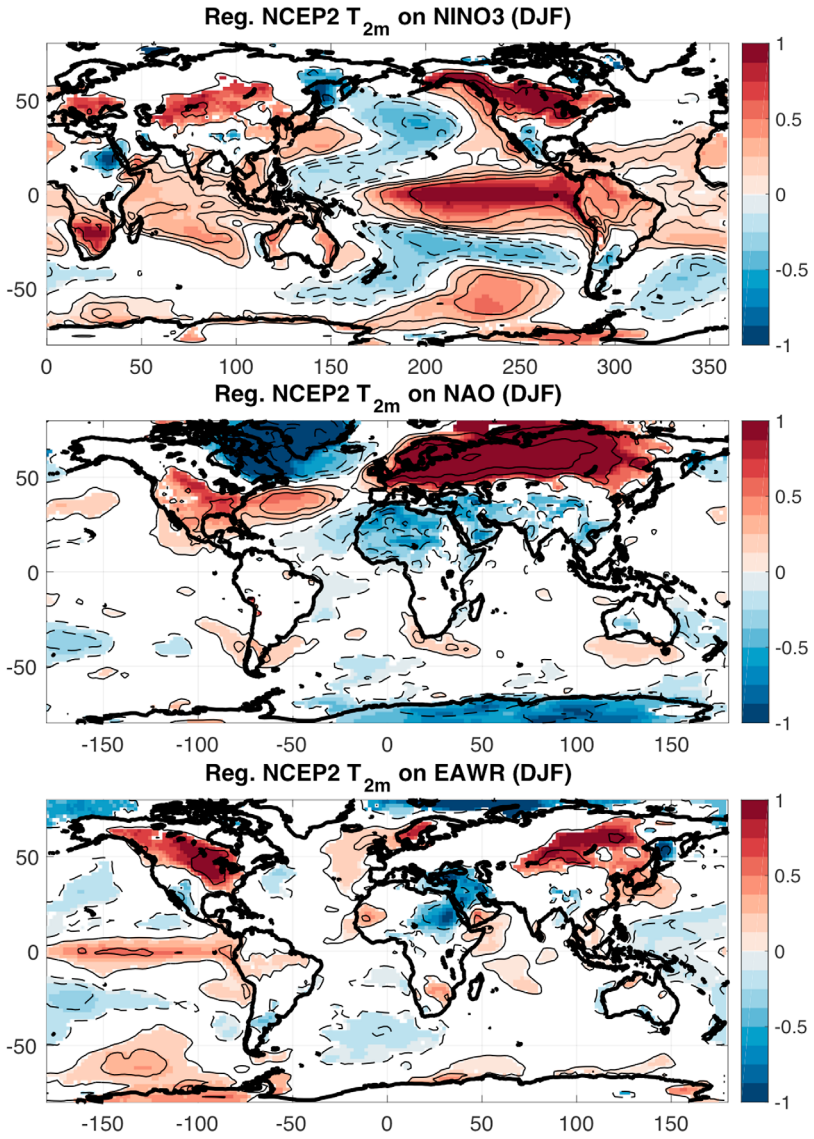

Figure 18. Boreal winter 2 m surface air temperature from the NCEP2 reanalysis regressed onto (°C) (color shading) and correlated with (black contours) (top) the boreal winter NINO3 index, (center) the boreal winter NAO index, and (bottom) the boreal winter EAWR index. Regression values significant at the 80% confidence level are shown (to emphasize large-scale patterns). Correlation coefficients are contoured every 0.2 with the zero contour omitted.

Neither of the aforementioned local wind anomalies emerging by statistical analysis with ENSO and NAO indices are intuitively linked to the dynamics or teleconnections associated with ENSO and NAO themselves. This raises the interesting question of whether there is a role for a local positive feedback triggered by the large-scale surface flux forcing such that the local wind field responds to the initial change in SST and serves to amplify that SST perturbation through enhanced surface flux anomalies and/or ocean circulation changes (such as overturning strength and upwelling). Sensitivity experiments with a regional atmospheric general circulation model (AGCM) or a regional coupled model may be able to demonstrate such a feedback.

To conclude the examination of possible regional and remote forcing mechanisms of the interannual variability of wintertime SST in the Red Sea, we briefly demonstrate the potential predictability of SST assuming reliable predictions of seasonal NINO3 and NAO values (Figure 20). Since the positive phase of ENSO is associated with warm SST anomalies in the southern Red Sea, and the positive phase of NAO is associated with cool SST anomalies in the northern Red Sea, and both of those results together describe an enhancement of the climatological mean meridional SST gradient, we first report correlations between those two indices

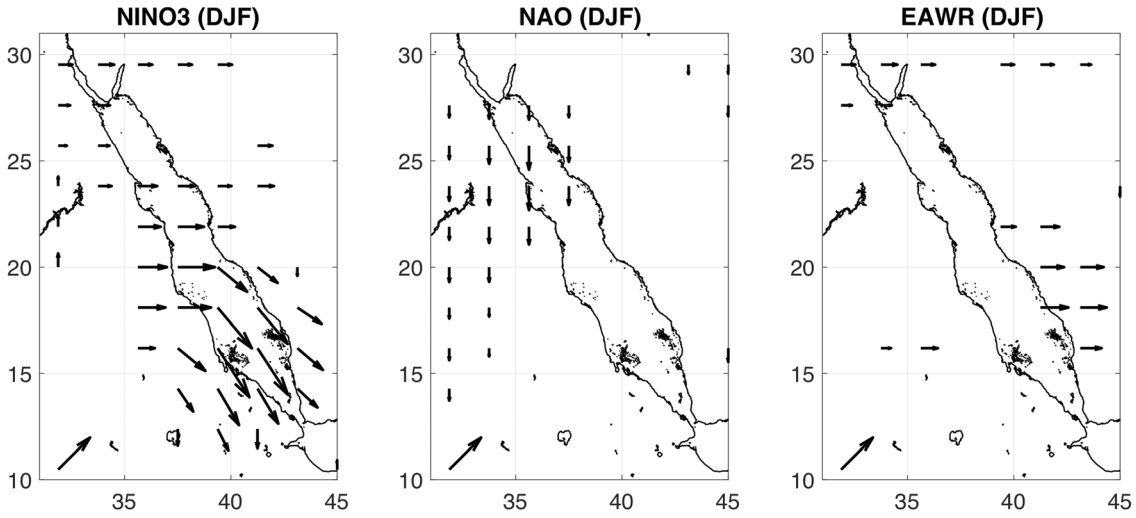

Figure 19. Boreal winter 10 m wind from the NCEP2 reanalysis regressed onto boreal winter (left) NINO3, (center) NAO, and (right) EAWR. Only values significant at the 99% confidence level are shown. A scale vector of (0.5, 0.5) m/s is provided in the lower-left corner.

independently against the gradient mode. The correlations with NINO3 and NAO are 0.45 and 0.34, respectively. However, when the two indices are simply normalized and summed, the resulting ENSO + NAO index yields a correlation coefficient of 0.55, which is statistically significant at the 95% confidence level.

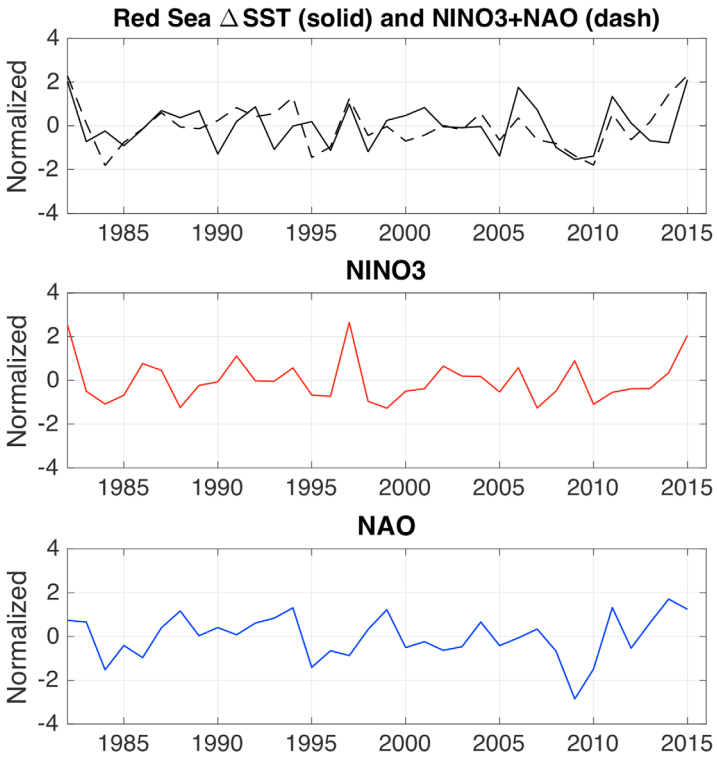

Figure 20. Meridional SST gradient within the Red Sea using 20°N as the boundary between the northern and southern Red Sea (black solid), sum of the normalized NINO3 and NAO indices (black dashed), NINO3 (red) and NAO (blue). All time series are for boreal winter (DJF) and are normalized. Correlations for NINO3, NAO, and their sum with the meridional SST gradient are 0.45, 0.34, and 0.55, respectively (all of which are statistically significant at the 95% confidence level).

4. Summary and Discussion

There is excellent agreement between the NOAA Optimal Interpolation (OI) v2 data product and shorter but higher-resolution ones such as MODIS; a detailed analysis of interannual variability was thus presented based on the 0.25° NOAA OI v2 data set from 1982 to 2016. The strongest interannual variability of SST is among wintertime seasonal means. Two dominant statistical modes of interannual variability (a whole-sea mode and ~meridional gradient mode (i.e., gradient along the major axis of the sea)) were identified by multiple lines of objective analysis. Regional surface air temperature and local winds both appear to play a role in driving the whole-sea mode. The East Atlantic/Western Russia pattern is a dominant factor in the wintertime SST variability across a broad area covering more than a quarter of the Red Sea, which appears to be independent of ENSO and NAO despite ENSO and the EAWR having a modest correlation. Although the global teleconnection patterns associated with ENSO and NAO both include surface air temperature and wind anomalies in the Red Sea region that would, based on first principles, lead to SST anomalies of the observed sign, observations alone are insufficient to diagnose which mechanism is most important in either case. Nevertheless, a statistical reconstruction of the meridional SST gradient in the Red Sea based on the linear combination of ENSO and NAO is significantly correlated ($r = 0.55$) with the observed time series.

Papadopoulos et al. (2015) indicated that the extremely cool conditions that occur in the north during winter may be enhanced not only by the air-sea exchange, but also by the cyclonic circulation that occurs in the north. Both Papadopoulos et al. (2015) and Acker et al. (2008) show both an annual increase during the winter months, but also that there is interannual variability. The highest MODIS-measured

chlorophyll in the northern Red Sea coincided with an anomalously cool winter in early 2012 (Papadopoulos et al., 2015), the mechanisms of which were recently examined by Gittings et al. (2018). Thus, the role of this interannual variability not only in affecting the direct air-sea flux and convective mixing, but also in driving the dynamics of the cyclonic circulation in the northern Red Sea that may enhance the upward flux of water from intermediate depths.

It remains an open question whether the surface wind signal associated with the gradient mode a *driver of* or a *response to* the meridional SST gradient that develops and fluctuates in the Red Sea. In other words, do the NAO and ENSO independently drive the northern and southern SST, respectively, which is then manifest as a meridional SST gradient that varies effectively randomly in time, and the local winds simply respond? More research, particularly regional modeling (e.g., OGCM-surface forcing sensitivity experiments, AGCM-SST perturbation experiments, and high-resolution coupled modeling), is needed to determine the role of feedbacks and, more generally, quantitatively diagnose the local processes (e.g., surface fluxes, horizontal advection, upwelling, mixing, overturning circulation, etc.) through which both the regional and large-scale/remote mechanisms are driving the observed interannual variations in SST.

Acknowledgments
K.B.K. acknowledges support from the Cooperative Institute for Research in Environmental Sciences (CIRES) Innovative Research Program (IRP). B.H.J. was funded by King Abdullah University of Science and Technology (KAUST). All sea surface temperature (SST) data sets used in this study are freely available via the URLs provided in section 2. NCEP/DOE Atmospheric Reanalysis II data were downloaded from the NOAA/ESRL/PSD web page at www.esrl.noaa.gov/psd/data/gridded/. ENSO, NAO, and EAWR indices were downloaded from NOAA/NWS/NCEP/CPC web pages at www.cpc.ncep.noaa.gov/data/indices/sstoi.indices, www.cpc.ncep.noaa.gov/products/precip/CWlink/pna/norm.nao.monthly.b5001.current.ascii, and ftp://ftp.cpc.ncep.noaa.gov/wd52dg/data/indices/eawr_index.tim, respectively.

References

Abualnaja, Y., Papadopoulos, V. P., Josey, S. A., Hoteit, I., Kontoyiannis, H., & Raitsos, D. E. (2015). Impacts of climate modes on air-sea heat exchange in the Red Sea. *Journal of Climate*, *28*(7), 2665–2681. https://doi.org/10.1175/JCLI-D-14-00379.1

Acker, J., Leptoukh, G., Shen, S., Zhu, T., & Kempler, S. (2008). Remotely-sensed chlorophyll a observations of the northern Red Sea indicate seasonal variability and influence of coastal reefs. *Journal of Marine Systems*, *69*(3–4), 191–204. https://doi.org/10.1016/j.jmarsys.2005.12.006

Barnston, A. G., & Livezey, R. E. (1987). Classification, seasonality and persistence of low-frequency atmospheric circulation patterns. *Monthly Weather Review*, *115*, 1083–1126.

Bjerknes, J. (1969). Atmospheric teleconnections from the equatorial pacific. *Journal of Physics Oceanography*, *97*(3), 163–172.

Björnsson, H., & Venegas, S. A. (1996). A manual for EOF and SVD analyses of climatic data (C2GCR Report 97-1, 54 pp.). Retrieved from http://www.geog.mcgill.ca/gec3/wp-content/uploads/2009/03/Report-no.-1997-1.pdf, accessed 12 July 2017.

Bower, A. S., & Farrar, J. T. (2015). Air-sea interaction and horizontal circulation in the Red Sea. In Rasul, N. M. A. & Stewart, I. C. F. (Eds.), *The Red Sea: The formation, morphology, oceanography and environment of a young ocean basin* (pp. 329–342). Berlin, Heidelberg: Springer. https://doi.org/10.1007/978-3-662-45201-1_19

Cantin, N. E., Cohen, A. L., Karnauskas, K. B., Tarrant, A. M., & McCorkle, D. C. (2010). Ocean warming slows coral growth in the central Red Sea. *Science*, *329*(5989), 322–325. https://doi.org/10.1126/science.1190182

Casey, K. S., Brandon, T. B., Cornillon, P., & Evans, R. (2010). The past, present and future of the AVHRR pathfinder SST program. In Barale, V., Gower, J. F. R., & Alberotanza, L. (Eds.), *Oceanography from space*. Berlin, Germany: Springer. https://doi.org/10.1007/978-90-481-8681-5_16

Churchill, J. H., Bower, A. S., McCorkle, D. C., & Abualnaja, Y. (2014). The transport of nutrient-rich Indian Ocean water through the Red Sea and into coastal reef systems. *Journal of Marine Research*, *72*, 165–181.

Dasari, H. P., Langodan, S., Viswanadhapalli, Y., Vadlamudi, B. R., Papadopoulos, V. P., & Hoteit, I. (2017). ENSO influence on the interannual variability of the Red Sea convergence zone and associated rainfall. *International Journal of Climatology*, *38*, 761–775. https://doi.org/10.1002/joc.5208

Dreano, D., Raitsos, D. E., Gittings, J., Krokos, G., & Hoteit, I. (2016). The Gulf of Aden intermediate water intrusion regulates the southern Red Sea summer phytoplankton blooms. *PLoS One*, *11*(12), e0168440. https://doi.org/10.1371/journal.pone.0168440

Eladawy, A., Nadaoka, K., Negm, A., Abdel-Fattah, S., Hanafy, M., & Shaltout, M. (2017). Characterization of the northern Red Sea's oceanic features with remote sensing data and outputs from a global circulation model. *Oceanologia*, *59*(3), 213–237. https://doi.org/10.1016/j.oceano.2017.01.002

Felis, T., Pätzold, J., Loya, Y., Fine, M., Nawar, A. H., & Wefer, G. (2000). A coral oxygen isotope record from the northern Red Sea documenting NAO, ENSO, and North Pacific teleconnections on Middle East climate variability since the year 1750. *Paleoceanography*, *15*(6), 679–694. https://doi.org/10.1029/1999PA000477

Gittings, J. A., Raitsos, D. E., Krokos, G., & Hoteit, I. (2018). Impacts of warming on phytoplankton abundance and phenology in a typical tropical marine ecosystem. *Scientific Reports*, *8*, 2240. https://doi.org/10.1038/s41598-018-20560-5

Kanamitsu, M., Ebisuzaki, W., Woollen, J., Yang, S., Hnilo, J. J., Fiorino, M., et al. (2002). NCEP-DOE AMIP-II Reanalysis (R-2). *Bulletin of the American Meteorological Society*, *83*, 1631–1643. https://doi.org/10.1175/BAMS-83-11-1631

Kilpatrick, K. A., Podestá, G., Walsh, S., Williams, E., Halliwell, V., Szczodrak, M., et al. (2015). A decade of sea surface temperature from MODIS. *Remote Sensing of Environment*, *165*, 27–41.

Langodan, S., Cavaleri, L., Vishwanadhapalli, Y., Pomaro, A., Bertotti, L., & Hoteit, I. (2017). The climatology of the Red Sea—Part 1: The wind. *International Journal of Climatology*, *37*, 4509–4517. https://doi.org/10.1002/joc.5103

Nandkeolyar, N., Raman, M., & Kiran, G. S., & Ajai, (2013). Comparative analysis of sea surface temperature pattern in the Eastern and Western Gulfs of Arabian Sea and the Red Sea in recent past using satellite data. *International Journal of Oceanography*, *2013*, 501602. https://doi.org/10.1155/2013/501602

Papadopoulos, V. P., Abualnaja, Y., Josey, S. A., Bower, A., Raitsos, D. E., Kontoyiannis, H., et al. (2013). Atmospheric forcing of the winter air-sea heat fluxes over the Northern Red Sea. *Journal of Climate*, *26*, 1685–1701. https://doi.org/10.1175/JCLI-D-12-00267.1

Papadopoulos, V. P., Zhan, P., Sofianos, S. S., Raitsos, D. E., Qurban, M., Abualnaja, Y., et al. (2015). Factors governing the deep ventilation of the Red Sea. *Journal of Geophysical Research: Oceans*, *120*, 7493–7505. https://doi.org/10.1002/2015JC010996

Raitsos, D. E., Hoteit, I., Prihartato, P. K., Chronis, T., Triantafyllou, G., & Abualnaja, Y. (2011). Abrupt warming of the Red Sea. *Geophysical Research Letters*, *38*, L14601. https://doi.org/10.1029/2011GL047984

Raitsos, D. E., Yi, X., Platt, T., Racault, M.-F., Brewin, R. J. W., Pradhan, Y., et al. (2015). Monsoon oscillations regulate fertility of the Red Sea. *Geophysical Research Letters*, *42*, 855–862. https://doi.org/10.1002/2014GL062882

Reynolds, R. W., Smith, T. M., Liu, C., Chelton, D. B., Casey, K. S., & Schlax, M. G. (2007). Daily high-resolution-blended analyses for sea surface temperature. *Journal of Climate*, *20*, 5473–5496. https://doi.org/10.1175/2007JCLI1824.1

Sofianos, S. S., & Johns, W. E. (2002). An Oceanic General Circulation Model (OGCM) investigation of the Red Sea circulation, 1. Exchange between the Red Sea and the Indian Ocean. *Journal of Geophysical Research*, *107*(C11), 3196. https://doi.org/10.1029/2001JC001184

Sofianos, S. S., & Johns, W. E. (2003). An Oceanic General Circulation Model (OGCM) investigation of the Red Sea circulation: 2. Three-dimensional circulation in the Red Sea. *Journal of Geophysical Research*, *108*(C3), 3066. https://doi.org/10.1029/2001JC001185

Sofianos, S. S., & Johns, W. E. (2007). Observations of the summer Red Sea circulation. *Journal of Geophysical Research*, *112*, C06025. https://doi.org/10.1029/2006JC003886

Sofianos, S., & Johns, W. E. (2017). The summer circulation in the Gulf of Suez and its influence in the Red Sea thermohaline circulation. *Journal of Physics Oceanography*, *47*, 2047–2053.

Visbeck, M. H., Hurrell, J. W., Polvani, L., & Cullen, H. M. (2001). The North Atlantic Oscillation: Past, present, and future. *Proceedings of the National Academy of Sciences of the United States of America*, *98*, 12,876–12,877.

Wafar, M., Qurban, M. A., Ashraf, M., Manikandan, K. P., Flandez, A. V., & Balala, A. C. (2016). Patterns of distribution of inorganic nutrients in Red Sea and their implications to primary production. *Journal of Marine Systems*, *156*, 86–98. https://doi.org/10.1016/j.jmarsys.2015.12.003

Wentz, F. J., Gentemann, C., & Hilburn, K. A. (2015a). *Remote sensing systems TRMM TMI monthly environmental suite on 0.25 deg grid, Version 7.1*. Santa Rosa, CA: Remote Sensing Systems. Retrieved from www.remss.com/missions/tmi, accessed 12 July 2017.

Wentz, F. J., Meissner, T., Scott, J., & Hilburn, K. A. (2015b). *Remote sensing systems GPM GMI monthly environmental suite on 0.25 deg grid, Version 8.1*. Santa Rosa, CA: Remote Sensing Systems. Retrieved from www.remss.com/missions/gmi, accessed 12 July 2017.

Wessel, P., & Smith, W. H. F. (1996). A global, self-consistent, hierarchical, high-resolution shoreline database. *Journal of Geophysical Research*, *101*, 8741–8743.

Worley, S. J., Woodruff, S. D., Reynolds, R. W., Lubker, S. J., & Lott, N. (2005). ICOADS release 2.1 data and products. *International Journal of Climatology*, *25*, 823–842.

Yao, F., Hoteit, I., Pratt, L. J., Bower, A. S., Köhl, A., Gopalakrishnan, G., et al. (2014b). Seasonal overturning circulation in the Red Sea: 2. Winter circulation. *Journal of Geophysical Research: Oceans*, *119*, 2263–2289. https://doi.org/10.1002/2013JC009331

Yao, F., Hoteit, I., Pratt, L. J., Bower, A. S., Zhai, P., Köhl, A., et al. (2014a). Seasonal overturning circulation in the Red Sea: 1. Model validation and summer circulation. *Journal of Geophysical Research: Oceans*, *119*, 2238–2262. https://doi.org/10.1002/2013JC009004